photonics

MDPI

Tutorial

Spatial Ensemble Mapping for Coded Aperture Imaging—A Tutorial

Narmada Joshi [1,†], Agnes Pristy Ignatius Xavier [1,2,†], Shivasubramanian Gopinath [1], Vipin Tiwari [1] and Vijayakumar Anand [1,3,*]

[1] Institute of Physics, University of Tartu, W. Ostwaldi 1, 50411 Tartu, Estonia; narmada@ut.ee (N.J.); agnes.pristy.ignatius.xavier@ut.ee (A.P.I.X.); shivasubramanian.gopinath@ut.ee (S.G.); vipin.tiwari@ut.ee (V.T.)
[2] School of Electrical and Computer Engineering, Ben Gurion University of the Negev, Beer-Sheva 8410501, Israel
[3] Optical Sciences Center, Swinburne University of Technology, Melbourne 3122, Australia
* Correspondence: vijayakumar.anand@ut.ee
† These authors contributed equally to this work.

Abstract: Coded aperture imaging (CAI) is a well-established computational imaging technique consisting of two steps, namely the optical recording of an object using a coded mask, followed by a computational reconstruction using a computational algorithm using a pre-recorded point spread function (PSF). In this tutorial, we introduce a simple yet elegant technique called spatial ensemble mapping (SEM) for CAI that allows us to tune the axial resolution post-recording from a single camera shot recorded using an image sensor. The theory, simulation studies, and proof-of-concept experimental studies of SEM-CAI are presented. We believe that the developed approach will benefit microscopy, holography, and smartphone imaging systems.

Keywords: coded aperture imaging; incoherent imaging; coded aperture; diffractive optics; holography; interferenceless coded aperture correlation holography

Citation: Joshi, N.; Ignatius Xavier, A.P.; Gopinath, S.; Tiwari, V.; Anand, V. Spatial Ensemble Mapping for Coded Aperture Imaging—A Tutorial. *Photonics* **2024**, *11*, 1174. https://doi.org/10.3390/photonics11121174

Received: 11 November 2024
Revised: 9 December 2024
Accepted: 11 December 2024
Published: 13 December 2024

1. Introduction

Computational imaging (CI) is a rapidly evolving field of research with incredible capabilities [1]. Coded aperture imaging is one of the oldest sub-fields of CI, developed to overcome the challenges associated with manufacturing lenses for non-visible regions of the electromagnetic spectrum such as X-rays and Gamma rays [2–4]. In CAI, the light from an object is modulated by a coded mask (CM), and the response to object intensity (I_{ROI}) is recorded by an image sensor. Like any imaging system, CAI involves a calibration step where the point spread function (I_{PSF}) is recorded using the CM. The image of the object is reconstructed by processing I_{PSF} with I_{ROI} using a computational reconstruction algorithm. While without a doubt, CAI enabled imaging for extreme wavelengths without a lens, the quality of images obtained from CAI after the above-described multiple steps did not reach the level of that obtained from a lens. Therefore, CAI evolved over the years, with developments in two directions, namely towards an advanced CM and a computational algorithm. Some notable inventions along the direction of CMs are the developments of the Fresnel zone aperture [5], uniformly redundant array mask [6], modified uniformly redundant array mask [7], and scattering mask [8]. Similarly, many developments in computational reconstruction methods such as the phase-only filter [9], Weiner deconvolution (WD) [10], and Lucy–Richardson algorithm were developed [11,12].

In 2017, interferenceless coded aperture correlation holography (I-COACH) was developed, which extended CAI to 3D imaging along three spatial dimensions [13]. It must be noted that CAI along three dimensions (2D space and spectrum) was achieved much earlier [14]. When I-COACH was developed using a quasi-random phase mask, it was found that the existing computational reconstruction methods did not support reconstruction of an image with a high signal-to-noise ratio (SNR). This led to the development of numerous

computational reconstruction methods such as non-linear reconstruction (NLR) [15], the Lucy–Richardson–Rosen algorithm (LRRA) [16], and incoherent non-linear deconvolution with an iterative algorithm (INDIA) [17].

The development of I-COACH had a significant impact on the field of imaging and holography [2]. I-COACH was able to achieve imaging capabilities that were believed to be impossible in imaging technology. Some key developments include the development of a 4D imaging capability along 3D space and spectrum using a monochrome camera [18], extending the field-of-view beyond the limits of the image sensor [19], a synthetic aperture imaging system that requires scanning only along the periphery with a scanning ratio < 0.01 (scanning ratio = scanned area/total area) [20], and imaging resolution enhancement [21,22]. Recently, a new problem, 'tuning axial resolution independent of lateral resolution', has been addressed extensively using I-COACH techniques [23–26]. As of 2024, the above problem has been solved creatively, with capabilities to tune axial and spectral resolutions post-recording [27,28]. However, the above methods require multiple camera shots.

In this tutorial, we introduce a simple yet valuable technique called spatial ensemble mapping (SEM), where an ensemble of diverse diffraction patterns is mapped to different radii of the image sensor. Therefore, different areas of the image sensor have different axial correlation lengths affecting their respective resolutions along the longitudinal space while the lateral resolution remains the same. This is because, the numerical aperture (NA) which controls the lateral correlation lengths remains the same, yielding a lateral resolution independent of the area selection in the image sensor. Therefore, the developed approach allows one to tune the axial resolution post-recording from a single camera recording without affecting the lateral resolution. Moreover, this approach creates a new interdependency between the field of the image sensor and the axial resolution that does not exist in conventional imaging, as well as CAI. Direct as well as inverse relations between the area of the sensor and axial resolution can be obtained. While we demonstrate the SEM concept for axial resolution only, the developed method can be used to tune other imaging characteristics such as spectral resolution, lateral resolution, and 3D image location.

This manuscript consists of six sections. The methodology is presented in Section 2. In Section 3, simulation studies are presented. The experimental studies are presented in Section 4. The results are discussed in Section 5. The conclusions of the study and future perspectives are presented in the final section of the manuscript.

2. Materials and Methods

The proposed SEM-CAI consists of two components, namely the CM design and imaging process, as shown in Figure 1. In the CM design, the SEM concept is applied, where the phase functions of several diffractive elements with different axial propagation characteristics are mapped to different regions of the image sensor mutually exclusively—without spatial overlap. This is achieved by combining unique linear phases (LPs) with the phase functions of different diffractive elements. There are no rules on what diffractive elements are to be used, where to map the functions on the image sensor, and what relationship between the area of the image sensor and axial resolution is needed. All the above can be selected depending upon the requirements 'on-demand'.

In this study, three diffractive elements, namely a diffractive axicon and two Fresnel zone plates (FZPs) with different focal distances, are selected. The diffraction pattern generated by the axicon is mapped to the origin of the image sensor. The diffraction patterns from the FZPs are mapped at certain distances away from the center in the positive and negative sides along the horizontal direction. The above mapping was designed such that when the area of the recording is increased, the axial resolution is increased. When the area includes only the diffraction pattern of the axicon, a low axial resolution is obtained. When the area includes the diffraction patterns of the axicon and FZP1, then the axial resolution increases, and when the area includes all the diffraction patterns, then the axial resolution is increased further. The choice of diffraction pattern of the diffractive axicon at the origin and FZP diffraction patterns at the sides is based on the above rationale and the properties of the diffraction patterns. The diffraction pattern of a diffractive axicon has a larger area compared to the diffraction spots of FZPs, and therefore it is

placed at the center, and the FZP diffraction patterns are placed at the sides at different distances from the center. Now, when the central region of the recording is used, a low axial resolution is obtained as the diffraction pattern of a diffractive axicon is non-changing with depth. But when the region of recording is increased, it will include the diffraction pattern of one of the FZPs for one case, causing an increase in axial resolution. When the full area of the recording is used, all the diffraction patterns are included, and the highest axial resolution is obtained. It is possible to have grayscale masks that can increase the contribution of one of the diffraction patterns with respect to the other. The maximum axial resolution is given by the NA, ~λ/NA^2 [2]. The proposed SEM-CAI allows one to tune the axial resolution from a certain value to the maxima but cannot be used to achieve super axial resolution.

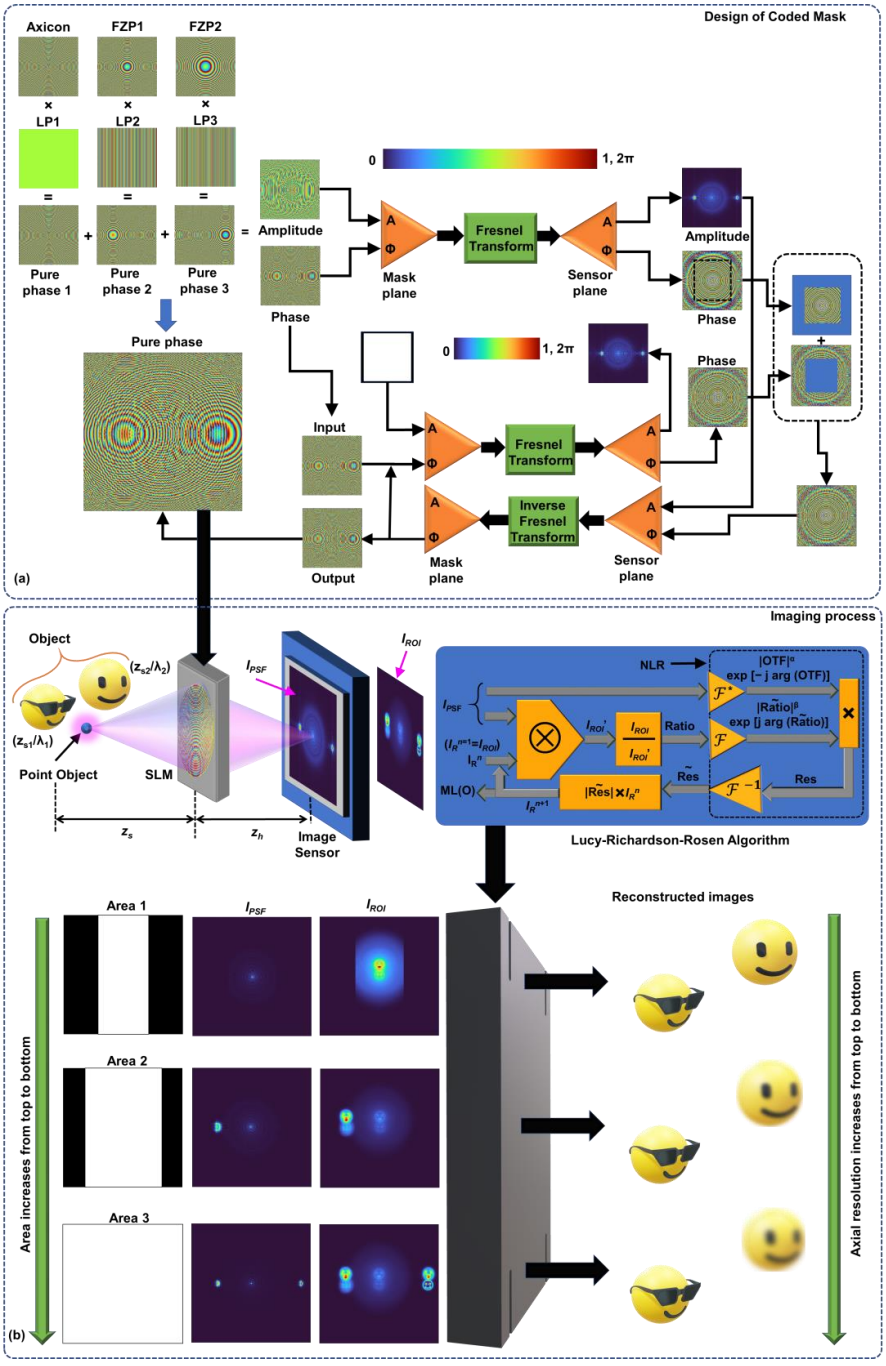

Figure 1. (**a**) Design of coded mask: Schematic of TAP-GSA. Three masks, a diffractive axicon, FZP1, and FZP2, are combined with unique LPs to map every diffraction pattern to a predefined area on the

image sensor. The resulting three masks are summed to obtain a complex function. The phase of the complex function and a uniform matrix are used as phase and amplitude constraints, respectively, in the mask domain. The amplitude distribution obtained by Fresnel propagation of the ideal complex function to the sensor domain is used as a constraint in the sensor domain. The phase distribution obtained at the sensor plane by Fresnel propagation is combined with the ideal phase distribution. The process is iterated to obtain a phase-only CM. A—amplitude; Φ—phase; FZP—Fresnel zone plate; LP—linear phase. (**b**) Imaging process: The CM is used to record I_{PSF} and I_{ROI}, and the above intensity distributions are mapped to different regions of the image sensor. With an increase in the area, the axial correlation lengths decrease. OTF—optical transfer function; n—number of iterations; ⊗—2D convolutional operator; $\Im^*$—refers to complex conjugate following a Fourier transform; $\Im^{-1}$—inverse Fourier transform; R^n is the nth solution and n is an integer, when n = 1, $I_R{}^n = I_{ROI}$; NLR—non-linear reconstruction; ML—maximum likelihood; α and β are varied from −1 to 1.

In this study, only spatially incoherent and temporally coherent light sources are considered. The phase functions of the diffractive axicon, FZP1, and FZP2 are given as $exp\left[-i2\pi\Lambda^{-1}R\right]$, $exp\left[-i\pi(\lambda f_1)^{-1}R^2\right]$, and $exp\left[-i\pi(\lambda f_2)^{-1}R^2\right]$, respectively, where Λ is the period of the axicon, $R = \left(x^2+y^2\right)^{1/2}$, and f_1 and f_2 are the focal distances of FZP1 and FZP2, respectively. The three LPs assigned to the above three masks are $LP(k) = exp\left[i2\pi(\lambda)^{-1}(a_k x + b_k y)\right]$, where k = 1, 2, and 3. The above LPs are combined with the phase functions of diffractive elements as $\Psi_{CM} = exp\left[-i2\pi\Lambda^{-1}R\right] \times LP(k=1) + exp\left[-i\pi(\lambda f_1)^{-1}R^2\right] \times LP(k=2) + exp\left[-i\pi(\lambda f_2)^{-1}R^2\right] \times LP(k=3)$, resulting in a complex function. A recently developed computational algorithm named transport of amplitude into phase based on Gerchberg–Saxton algorithm (TAP-GSA) is used to convert the complex function Ψ_{CM} into a phase-only function as shown in Figure 1a [29]. In TAP-GSA, there are two planes of interest: the mask plane and sensor plane. In the first step, a complex mask Ψ_{CM} with both amplitude and phase components is designed at the mask plane, and the amplitude and phase generated at the sensor plane by forward propagation is calculated using a Fresnel transform. These generated amplitude and phase functions will be referred to as the ideal amplitude and phase matrices. The goal of TAP-GSA is to convert Ψ_{CM} into a phase-only function, and therefore at the mask plane, a uniform amplitude matrix, $M(x,y) = 1$, for all values of x and y is created as a constraint, and the phase matrix of Ψ_{CM}, i.e., $\exp[i\ arg(\Psi_{CM})]$ is used as an initial starting point. The phase-only matrix $\exp[i\ arg(\Psi_{CM})]$ is forward-propagated using a Fresnel transform to obtain the complex amplitude matrix at the sensor plane. At the sensor plane, the obtained amplitude matrix is replaced by the ideal amplitude matrix, and the obtained phase matrix is partially replaced by the ideal phase matrix. The number of pixels replaced in the phase matrix to the total number of pixels is called the degrees of freedom. The resulting complex amplitude matrix after applying the above constraints is backpropagated to the mask plane, and once again, the amplitude matrix is replaced by a uniform matrix, $M(x,y) = 1$, for all values of x and y, and the phase matrix is retained. This process is iterated until the algorithm converges to a non-changing matrix.

Therefore, the final CM obtained from the TAP-GSA can be expressed as $\Psi_{CM} \approx exp(i\gamma)$. The resulting phase-only CM is used for the next step—the imaging process. The application of the TAP-GSA is crucial to the implementation of SEM as the alternative random multiplexing method developed for Fresnel incoherent correlation holography (FINCH) results in speckle noises affecting the overall tunability of axial resolution [30,31]. When the TAP-GSA was implemented for FINCH, instead of random multiplexing, a significant improvement in SNR and light throughput was observed. The commented MATLAB code for implementing the TAP-GSA is provided in the Supplementary Materials (Supplementary_code1.txt) [32].

The imaging process shown in Figure 1b in the next step can be mathematically expressed as follows: A point object is considered in the object domain $(\bar{r}_s, z_s)$ from the CM. The complex amplitude reaching the CM is given as $\sqrt{I_s}C_1 L\left(\frac{\bar{r}_s}{z_s}\right) Q\left(\frac{1}{z_s}\right)$, where $\sqrt{I_s}$ is the amplitude, Q is a quadratic phase function given as $Q(a) = exp\left[i\pi a\lambda^{-1}R^2\right]$, L is the linear phase function given as $L\left(\frac{\bar{s}}{z}\right) = exp\left[i2\pi(\lambda z)^{-1}\left(s_x x + s_y y\right)\right]$, and C_1 is a complex

constant. The complex amplitude after the CM is given as $\sqrt{I_s}C_1L\left(\frac{\bar{r}_s}{z_s}\right)Q\left(\frac{1}{z_s}\right)\Psi_{CM}$, which is propagated by a distance of z_h and recorded by an image sensor whose intensity distribution is given as

$$I_{PSF}(\bar{r}_0;\bar{r}_s,z_s,\lambda)=\left|\sqrt{I_s}C_1L\left(\frac{\bar{r}_s}{z_s}\right)Q\left(\frac{1}{z_s}\right)\Psi_{CM}\bigotimes Q\left(\frac{1}{z_h}\right)\right|^2, \tag{1}$$

where '$\bigotimes$' is a 2D convolutional operator and $\bar{r}_0=(u,v)$ is the location vector in the sensor plane. However, unlike the previous developments of CAI and I-COACH, there is a new equality in the proposed approach which is

$$\begin{gathered}\left|\sqrt{I_s}C_1L\left(\frac{\bar{r}_s}{z_s}\right)Q\left(\frac{1}{z_s}\right)\Psi_{CM}\otimes Q\left(\frac{1}{z_h}\right)\right|^2\approx\\ \left|\sqrt{I_s}C_{11}L\left(\frac{\bar{r}_s}{z_s}\right)Q\left(\frac{1}{z_s}\right)exp\left[-i2\pi\Lambda^{-1}R\right]LP(k=1)\otimes Q\left(\frac{1}{z_h}\right)\right|^2+\\ \left|\sqrt{I_s}C_{12}L\left(\frac{\bar{r}_s}{z_s}\right)Q\left(\frac{1}{z_s}\right)exp\left[-i\pi(\lambda f_1)^{-1}R^2\right]LP(k=2)\otimes Q\left(\frac{1}{z_h}\right)\right|^2+\\ \left|\sqrt{I_s}C_{13}L\left(\frac{\bar{r}_s}{z_s}\right)Q\left(\frac{1}{z_s}\right)exp\left[-i\pi(\lambda f_2)^{-1}R^2\right]LP(k=3)\otimes Q\left(\frac{1}{z_h}\right)\right|^2,\end{gathered} \tag{2}$$

where C_{11}, C_{12}, C_{13} are complex constants. The above equality is possible because of SEM, which has a much deeper meaning. In Equation (1), there is self-interference $I=\left|\sum_m A_m\right|^2$ between the ensemble of optical fields, whereas the equality shown in Equation (2), has a unique behavior, $I=\sum_m|A_m|^2$, where A represents the ensemble of diffracted fields generated by the CM. In the first case, where there is self-interference, the nature of light is spatially incoherent and temporally coherent, which matches with the source specifications. In the second case, due to SEM, the fields generated by the CM that are mapped to different locations behave as if they are not coherent with respect to one another, even though derived from the same object point. This is a fundamental change through SEM that allows such a tunability. Equation (1) can be expressed as

$$I_{PSF}(\bar{r}_0;\bar{r}_s,z_s,\lambda)\approx I_{PSF1}(\bar{r}_0;\bar{r}_s,z_s,\lambda)+I_{PSF2}(\bar{r}_0;\bar{r}_s,z_s,\lambda)+I_{PSF3}(\bar{r}_0;\bar{r}_s,z_s,\lambda), \tag{3}$$

where I_{PSF1}, I_{PSF2}, and I_{PSF3} are PSFs of the axicon, FZP1, and FZP2, respectively. By selecting the area of the recordings, it is possible to control the contributions from the different diffractive elements. I_{PSF1} has a low sensitivity to changes in depth and wavelength, whereas I_{PSF2} and I_{PSF3} have a high sensitivity to changes in depth and wavelength as given by the numerical aperture NA. Therefore, when there is a change in depth and only the central region of the recording containing only the diffracted field of the axicon is considered, then the correlation curve given as $|I_{PSF1}(\bar{r}_0;\bar{r}_s,z_s)*I_{PSF1}(\bar{r}_0;\bar{r}_s,z_s+\Delta z)|$ will be as broad as $I_{PSF1}(\bar{r}_0;\bar{r}_s,z_s)\approx I_{PSF1}(\bar{r}_0;\bar{r}_s,z_s+\Delta z)$, where '*' is a 2D correlation operator. The same argument also applies to changes in wavelength. Let us consider the other cases when the area includes a diffracted field of an FZP in addition to that from an axicon; $|\{I_{PSF1}(\bar{r}_0;\bar{r}_s,z_s)+I_{PSF2}(\bar{r}_0;\bar{r}_s,z_s)\}*\{I_{PSF1}(\bar{r}_0;\bar{r}_s,z_s+\Delta z)+I_{PSF2}(\bar{r}_0;\bar{r}_s,z_s+\Delta z)\}|$ will be sharper than the previous case, as $I_{PSF2}(\bar{r}_0;\bar{r}_s,z_s)\neq I_{PSF2}(\bar{r}_0;\bar{r}_s,z_s+\Delta z)$. Once again, the above is true for the wavelength. In this way, the axial resolution can be tuned between the limits of axicon and lens, which are $\sim D\Lambda/2\lambda$ and $\sim\lambda/NA^2$, respectively, where D is the diameter of the CM [33–37].

The proposed SEM-CAI is a linear, shift-invariant system and therefore,

$$\begin{gathered}I_{PSF}(\bar{r}_0;\bar{r}_s,z_s,\lambda)=I_{PSF1}\left(\bar{r}_0-\tfrac{z_h}{z_s}\bar{r}_s;0,z_s,\lambda\right)+I_{PSF2}\left(\bar{r}_0-\tfrac{z_h}{z_s}\bar{r}_s;0,z_s,\lambda\right)+\\ I_{PSF3}\left(\bar{r}_0-\tfrac{z_h}{z_s}\bar{r}_s;0,z_s,\lambda\right).\end{gathered} \tag{4}$$

A 2D object with N points can be represented mathematically as a collection of N Delta functions given by

$$o(\bar{r}_s) = \sum_j^N a_j \delta(\bar{r} - \bar{r}_{s,j}), \tag{5}$$

where a_j's are constants. The response to object intensity based on the assumption that a spatially incoherent and temporally coherent light source is considered is given as

$$I_{ROI}(\bar{r}_0; z_s) = \sum_{j,k}^{N,3} a_j I_{PSF(k)}\left(\bar{r}_0 - \frac{z_h}{z_s}\bar{r}_{s,j}; 0, z_s\right). \tag{6}$$

There are numerous deconvolution methods that can be applied, and, in this study, LRRA and WD are used for reconstructing the object information as shown in Figure 1b. The $(n + 1)$th reconstructed image of LRRA is given as

$$I_R^{n+1} = I_R^n \left\{ \left(\frac{I_{ROI}}{I_R^n \otimes I_{PSF}} \right) \circledast I_{PSF} \right\}, \tag{7}$$

where '$\circledast$' indicates the NLR operation which is given as $\left| \mathcal{F}^{-1}\left\{ \left|\tilde{A}\right|^{\alpha} exp\left[i\, arg\left(\tilde{A}\right)\right] \left|\tilde{B}\right|^{\beta} exp\left[-i\, arg\left(\tilde{B}\right)\right] \right\} \right|$, where $\tilde{X}$ is the Fourier transform of X and A and B are the two matrices. The α and β are tuned between -1 and 1 to obtain the optimal entropy and a fast convergence. The LRRA has been thoroughly discussed in [16,17]. The algorithm is briefly summarized here. The LRRA begins with an initial guess solution of the object, which is the I_{ROI}. In principle, the initial guess can be any matrix, even random, but to improve the convergence, the initial guess is selected as I_{ROI}. This initial guess is convolved with I_{PSF} to obtain I_{ROI}', which will be I_{ROI} if the initial guess were the actual solution. The ratio between the recorded response to object intensity and obtained matrix, given as Ratio = I_{ROI}/I_{ROI}', is calculated. Then the Ratio is processed with I_{PSF} using NLR to obtain the Residue. The Residue is multiplied to the previous solution, which is the initial guess solution, to obtain the next solution ($n = 2$). This process is iterated until an optimal solution is obtained. During the reconstruction, the values of α and β are set to a value and are not changed once the iteration is started. The commented on MATLAB code is provided in the Supplementary Materials (Supplementary_code2.txt).

3. Simulation Results

The simulation studies were carried out in MATLAB software (version R2022a). A matrix size of 500 × 500 pixels, a pixel size $\Delta = 10$ µm, wavelength $\lambda = 632.8$ nm, object distance $z_s = 1$ m, and a recording distance (distance between CM and image sensor) $z_h = 0.2$ m were selected. Three grayscale diffractive elements were designed: an axicon with $\Lambda = 80$ µm with no linear phase ($a_k = b_k = 0$), FZP1 ($f_1 = 0.16$ m) ($a_k = -0.007$, $b_k = 0$), and FZP2 ($f_2 = 0.17$ m) ($a_k = 0.01$, $b_k = 0$). The phase images of the masks are shown in Figure 2a, Figure 2b, and Figure 2c, respectively. The linear phases are gratings that change the direction of light. Without the linear phases, all three diffraction patterns will be at the center of the image sensor. By adding different linear phases to different diffractive elements, the respective diffraction patterns experience different propagation directions, allowing them to map at different transverse locations on the image sensor.

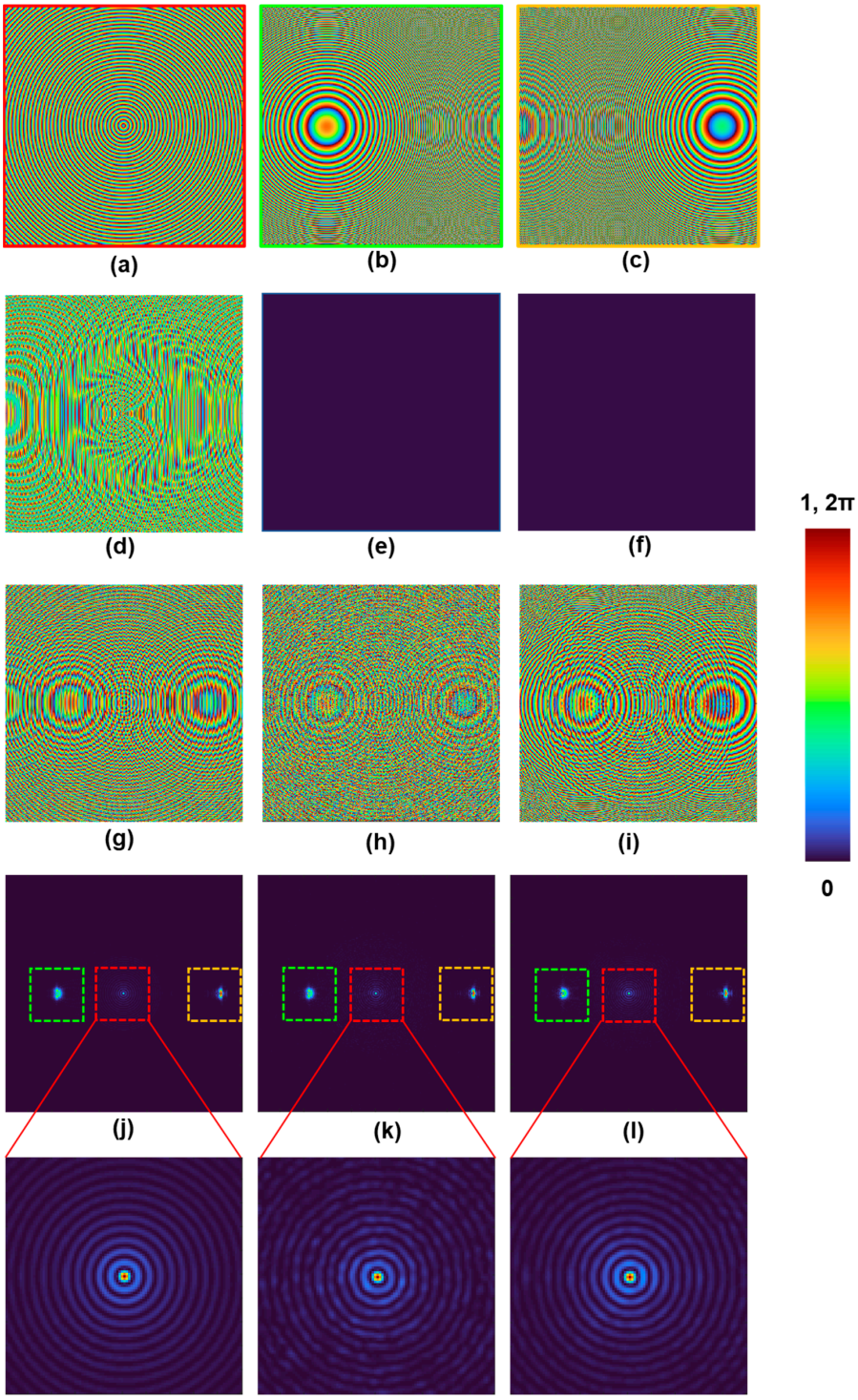

Figure 2. Simulation results for design and analysis of CM: Phase images of (**a**) diffractive axicon, (**b**) FZP1, (**c**) FZP2. Magnitude of CM obtained by (**d**) sum of phase functions of diffractive axicon, FZP1, and FZP2, (**e**) random multiplexing, and (**f**) TAP-GSA. Phase images of CM designed by (**g**) sum of phase functions of diffractive axicon, FZP1, and FZP2, (**h**) random multiplexing, and (**i**) TAP-GSA. Diffraction patterns obtained from (**j**) complex CM, (**k**) CM designed by random multiplexing, and (**l**) CM designed by TAP-GSA. The masks shown in (**a**–**c**) generate the respective intensity distributions as matched with the same color.

The magnitude of the CMs obtained by the sum of the three phase-only functions of the diffractive axicon, FZP1 with LP2, and FZP2 with LP3, random multiplexing, and

the TAP-GSA with a degree of freedom of 0.16 are shown in Figure 2d, Figure 2e, and Figure 2f, respectively. The phase of the CMs obtained by the sum of the above three phase functions, random multiplexing and the TAP-GSA with a degree of freedom of 0.16 are shown in Figure 2g, Figure 2h, and Figure 2i, respectively. The diffraction pattern obtained at a distance of 0.2 m from the CM for the above three cases are shown in Figure 2j, Figure 2k, and Figure 2l, respectively. The magnified regions of the intensity matrices for the above three cases show a reduced scattering noises with the TAP-GSA. It must be noted that the case of Figure 2j for a complex CM does not have any noise as it is the ideal CM. However, such a complex CM cannot be realized using the current state-of-the-art spatial light modulators, as they are either amplitude-only or phase-only modulators. Therefore, the complex CMs are converted into approximate amplitude-only or phase-only CMs. Random multiplexing is one such method that is used for approximating a complex CM by a phase-only CM. However, this approach results in substantial scattering noises and a low light throughput, as seen in Figure 2k. This problem was addressed in our recent study, and a new approach, the TAP-GSA, was developed to approximate a complex CM by a phase-only CM with significantly lower scattering noises and improved light throughput [29]. As seen in Figure 2l, the scattering noises are lower than those of the random multiplexing shown in Figure 2k. However, the scattering noises of Figure 2l are slightly higher than those of the ideal complex CM.

The axial behavior is simulated next. The I_{PSF} is simulated for different values of z_s and processed with I_{PSF} corresponding to a single value of z_s as $|I_{PSF}(\bar{r}_0;\bar{r}_s,z_s) * I_{PSF}(\bar{r}_0;\bar{r}_s,z_s+\Delta z)|$, where z_s = 1 m and Δz_s is tuned from −0.5 m to 0.5 m. The normalized curves of $|I_{PSF1}(\bar{r}_0;\bar{r}_s,z_s) * I_{PSF1}(\bar{r}_0;\bar{r}_s,z_s+\Delta z)|$ for six cases of masks applied to recordings are shown in Figure 3. The FWHM of the normalized curves for Masks 1 to 6 are 0.19 m, 0.15 m, 0.13 m, 0.09, 0.08, and 0.08, respectively, indicating a gradual increase in the axial resolution, with the maximum and minimum values corresponding to the axicon and lens, respectively. It can be seen that by selecting an appropriate mask, different strengths of axial correlation lengths can be contributed from different areas of the recordings, resulting in the desired effective axial resolution.

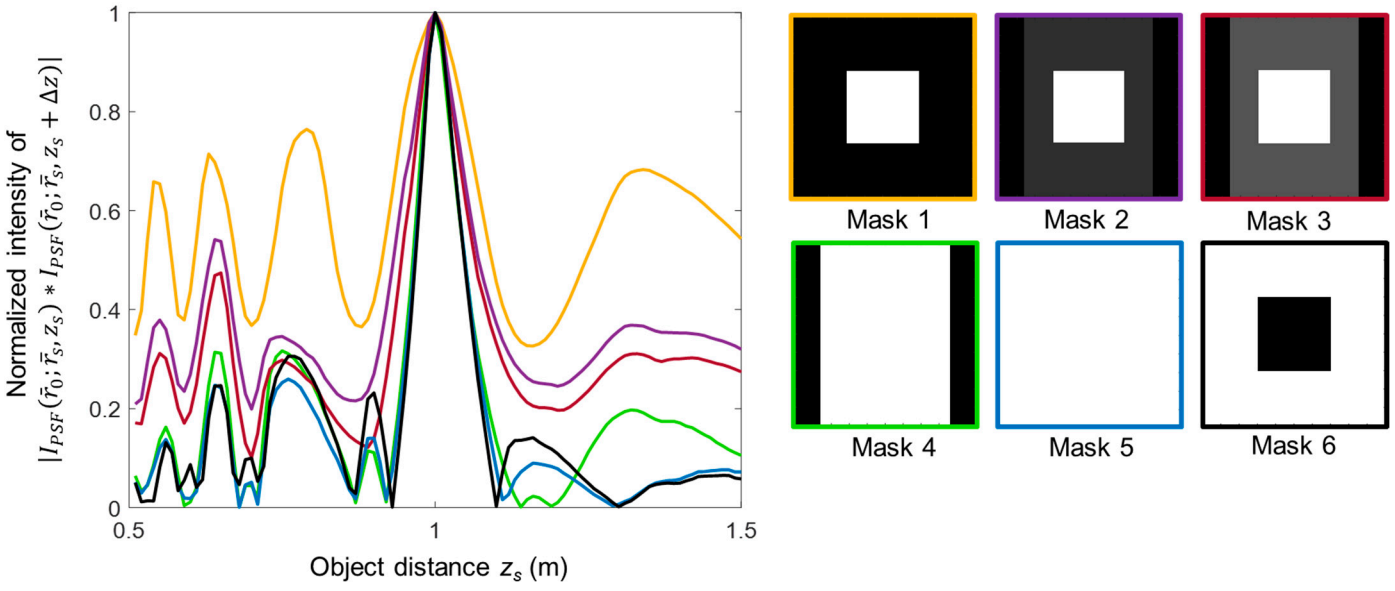

Figure 3. Simulation results of axial correlation curves for different masks applied to the recorded I_{PSF} and I_{ROI}. The gray region in Mask2 has a ratio of 0.33 to the white region, and Mask6 has a ratio of 0.25 to the white region. The color of the curves are matched with the border color of the masks. The axial resolution can be tuned between the limits of the axicon (yellow line) and a diffractive lens (black line).

The simulated optical experiments are discussed next. Two 'smiley' objects were selected for the study, as shown in Figure 4a,b. The two objects were separated by a distance of 20 cm. Even though there are clear variations in the curves shown in Figure 3 for different cases of the masks, in imaging it is challenging to observe minor changes in axial resolution. Therefore, for the simulation study, only three cases are considered, corresponding to Mask1, Mask2, and Mask4. The images of the simulated I_{PSF}s, I_{ROI}s, and I_Rs for Mask1, Mask2, and Mask4 are shown in Figure 4. From the results, it can be seen that the axial resolution increases from Mask1 to Mask4. The reconstructed second smiley object—test object 2—becomes more and more blurred with an increase in the axial resolution. For all the above cases, the LRRA is applied with three to five iterations, with $\alpha = 0$, $\beta = 0$ to 0.2. When the axial resolution is increased, the strength of the object's image in planes other than the plane of interest becomes weaker and blurred. In this simulation study, the plane of interest is where object 1 is located, and therefore with an increase in the axial resolution, the image of object 2 becomes more blurred and weaker in Figure 4k compared to Figure 4e,h. However, object 1 is expected to be focused for all three cases, as it is located in the plane of interest. The simulation results show that object 1 appears focused for all three cases.

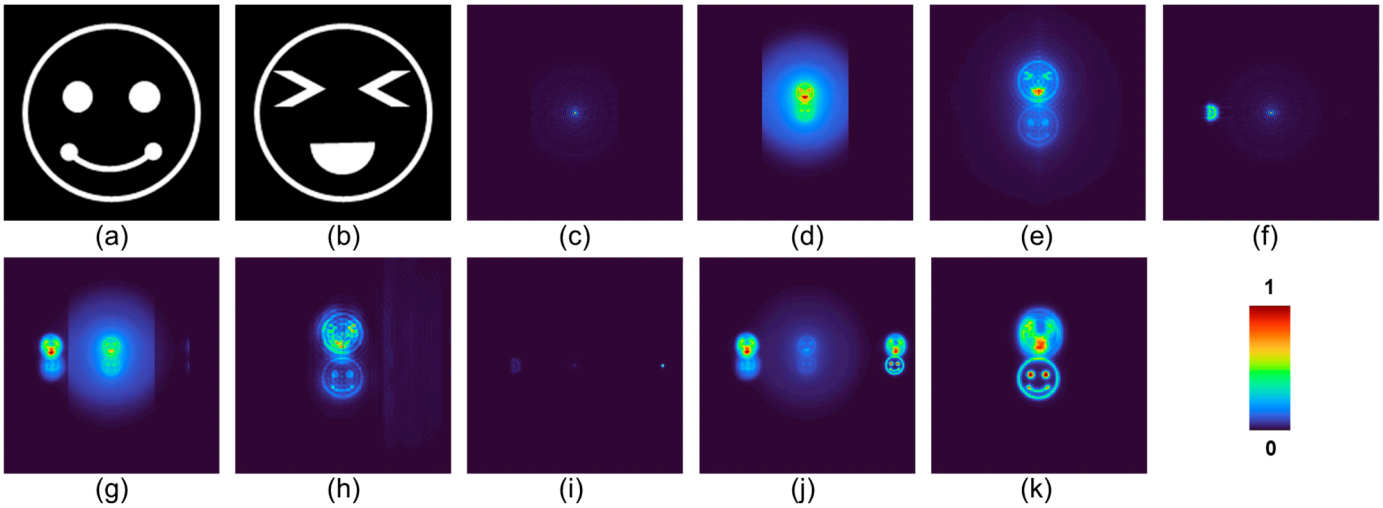

Figure 4. (**a**) Test object 1, (**b**) test object 2. Images of (**c**) $I_{PSF,}$ (**d**) $I_{ROI,}$ (**e**) I_R for Mask1. Images of (**f**) $I_{PSF,}$ (**g**) $I_{ROI,}$ (**h**) I_R for Mask2. Images of (**i**) $I_{PSF,}$ (**j**) $I_{ROI,}$ (**k**) I_R for Mask4.

4. Experiments

The schematic and a photograph of the experimental setup are shown in Figure 5a,b. The experimental setup includes the following optical components: a light emitting diode (LED) from Thorlabs with 940 mW power, operating at a wavelength of $\lambda = 660$ nm and a bandwidth of $\Delta\lambda = 20$ nm; two irises; polarizer; three refractive lenses (RLs) with focal lengths of $f = 3.5$ cm, $f = 5$ cm, and $f = 5$ cm; pinhole of size 50 µm; beam splitter (BS); Exulus-4K 1/M spatial light modulator (SLM) from Thorlabs with 3840 × 2160 pixels and a pixel size of 3.74 µm; and Zelux CS165MU/M monochrome image sensor with 1440 × 1080 pixels, with a pixel size of ~3.5 µm. It must be noted that the PSF is recorded using a point object such as a pinhole, and the light from the pinhole is spatially and temporally coherent. Since there is only one point, there is no difference between using a coherent or an incoherent source for illuminating a pinhole. However, an object with multiple points illuminated by an LED generates an object wave that is spatially incoherent but temporally coherent, just as the light from an LED.

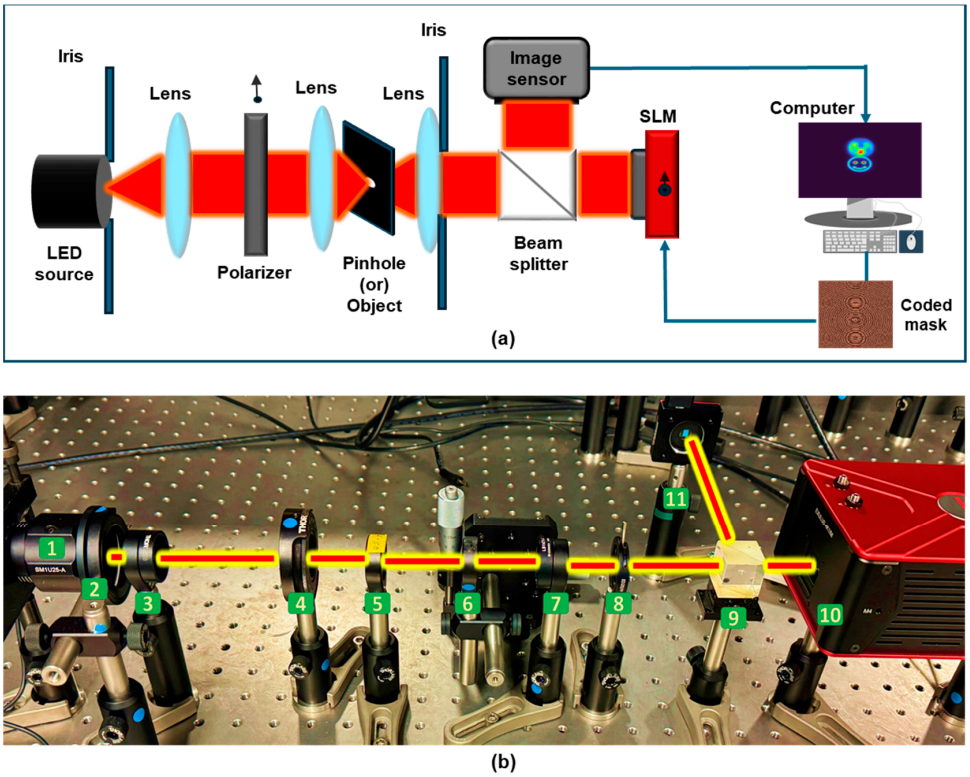

Figure 5. (**a**) Schematic and (**b**) photograph of experimental configuration. (1) LED, (2) iris, (3) refractive lens (f = 3.5 cm), (4) polarizer, (5) refractive lens (f = 5 cm), (6) object/pinhole, (7) refractive lens (f = 5 cm), (8) iris, (9) beam splitter, (10) spatial light modulator, (11) monochrome image sensor.

The light from the LED is controlled by an iris and collimated by an RL (f = 3.5 cm). The collimated beam is passed through a polarizer, which is oriented along the active axis of the SLM. Two objects are created by shifting a pinhole of 50 µm in horizontal and vertical directions. Object 1 (two points along the horizontal direction separated by 120 µm) and object 2 (two points along the vertical direction separated by 120 µm) are created. The object is critically illuminated by an RL (f = 5 cm). The light beam from the object is collimated by an RL (f = 5 cm), and the beam size is controlled by another iris. The collimated light beam enters the BS and is incident on the SLM. The CM is created by combining two FZPs (with a focal length of 16 cm) and one diffractive axicon (with Λ = 187 µm) using the TAP-GSA with a degree of freedom of 75% similar to the simulation study as shown in Figure 2i. The phase-only CM from the TAP-GSA is displayed on the SLM, which modulates the light beam, creating the diffraction spots of the two FZPs and diffractive axicon at predefined locations on the image sensor. The I_{PSF} and I_{ROI} are recorded by the image sensor located at a distance of 20 cm from the SLM. The I_{PSF} is recorded using a 50 µm pinhole. Object 1 and object 2 are recorded at two different depths, z_s = 5 cm and z_s = 5.4 cm, respectively. The object information is reconstructed by processing I_{PSF} and I_{ROI} using the LRRA. The experimentally recorded I_{PSF} and I_{ROI} are shown in Figures 6a and 6b, respectively. Two masks, Mask1 and Mask2, are applied to the recorded I_{PSF} and I_{ROI} and reconstructed. The images of Mask1 and Mask2 and the reconstructed images are shown in Figure 6c, Figure 6d, Figure 6e, and Figure 6f, respectively. The phase image of the CM generated using the TAP-GSA with degrees of freedom of 75% is shown in Figure 6g. Comparing the reconstruction results of Figure 6d,f, the axial resolution of Figure 6f is better than that of Figure 6d, demonstrating the tunability of axial resolution post-recording. In the case of Mask1 (Figure 6c), there is contribution only from the diffractive axicon, which has a long axial correlation length, resulting in a low axial resolution. In the case of Mask2 (Figure 6e), there is contribution from two FZPs and a diffractive axicon, resulting in a short axial

correlation length. The shorter correlation length for Mask2 arises due to the averaging effect of correlation lengths corresponding to the diffractive axicon and FZPs. However, in the above two cases, the lateral correlation length is the same, as the NA is constant for both cases. In all the above cases, the typical range of α, β and the number of iterations for LRRA are 0 to 0.4, 1, and 10 to 30, respectively. The experimental results are matched with the simulation results and validate the theory of SEM-CAI.

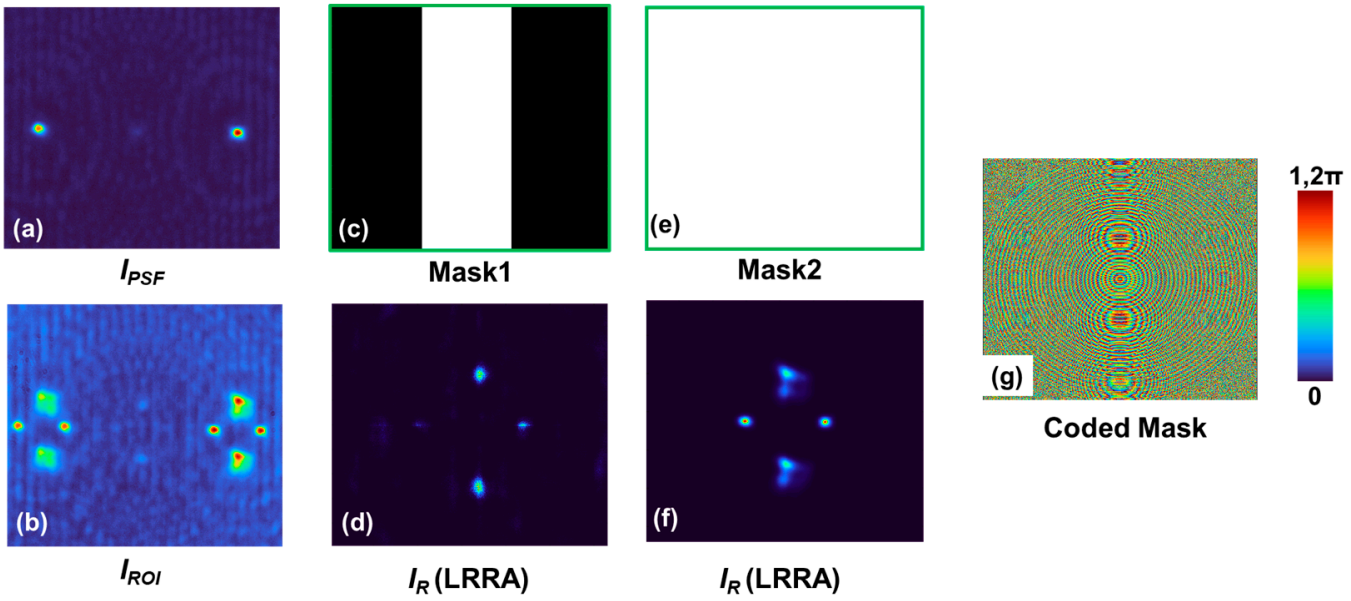

Figure 6. Experimentally recorded (**a**) I_{PSF}, (**b**) I_{ROI}. Images of (**c**) Mask1 and the (**d**) corresponding reconstruction. Images of (**e**) Mask2 and the (**f**) corresponding reconstruction. (**g**) Phase image of the CM designed by the TAP-GSA with 75% degrees of freedom.

5. Discussion

In this study, a simple yet useful technique called SEM has been introduced in CAI for tuning the axial resolution independent of lateral resolution post-recording. Like any new technique, an advancement is made here with SEM-CAI, with a compromise on the field of view. The above approach is suitable only for recording events and scenes with a limited field of view. The above understanding also gives rise to a question. Can direct imaging approaches be applied here by reducing the field of view and tiling different configurations along the x and y directions on the image sensor? This is impossible due to the interdependency between lateral and axial resolutions in direct imaging approaches. Even if that condition is relaxed, the direct imaging approach can allow only the discrete tuning of axial resolution along the tiled images. The interdependency between lateral and axial resolutions by NA will cause a change in lateral resolution also along the tiled images.

In terms of the developed SEM-CAI, even though it has been demonstrated only for tuning axial resolution independent of lateral resolution, the concept can be extended to tuning spectral resolution independent of lateral resolution as well. Simulation results for tuning spectral resolution post-recording using a monochrome sensor for three masks, Mask1, Mask2, and Mask4, were obtained. The spectral correlation curves obtained from $|I_{PSF}(\bar{r}_0;\bar{r}_s,z_s,\lambda) * I_{PSF}(\bar{r}_0;\bar{r}_s,z_s,\lambda+\Delta\lambda)|$ for a wavelength variation between 400 to 800 nm for the three masks are shown in Figure 7. As can be seen, the spectral resolution improves from Mask1 to Mask4. The same approach can also be used to tune the lateral resolution, which has not been discussed in [27,28] and, so far, is not possible after recording a picture or a video. However, a low lateral resolution does not have any useful application.

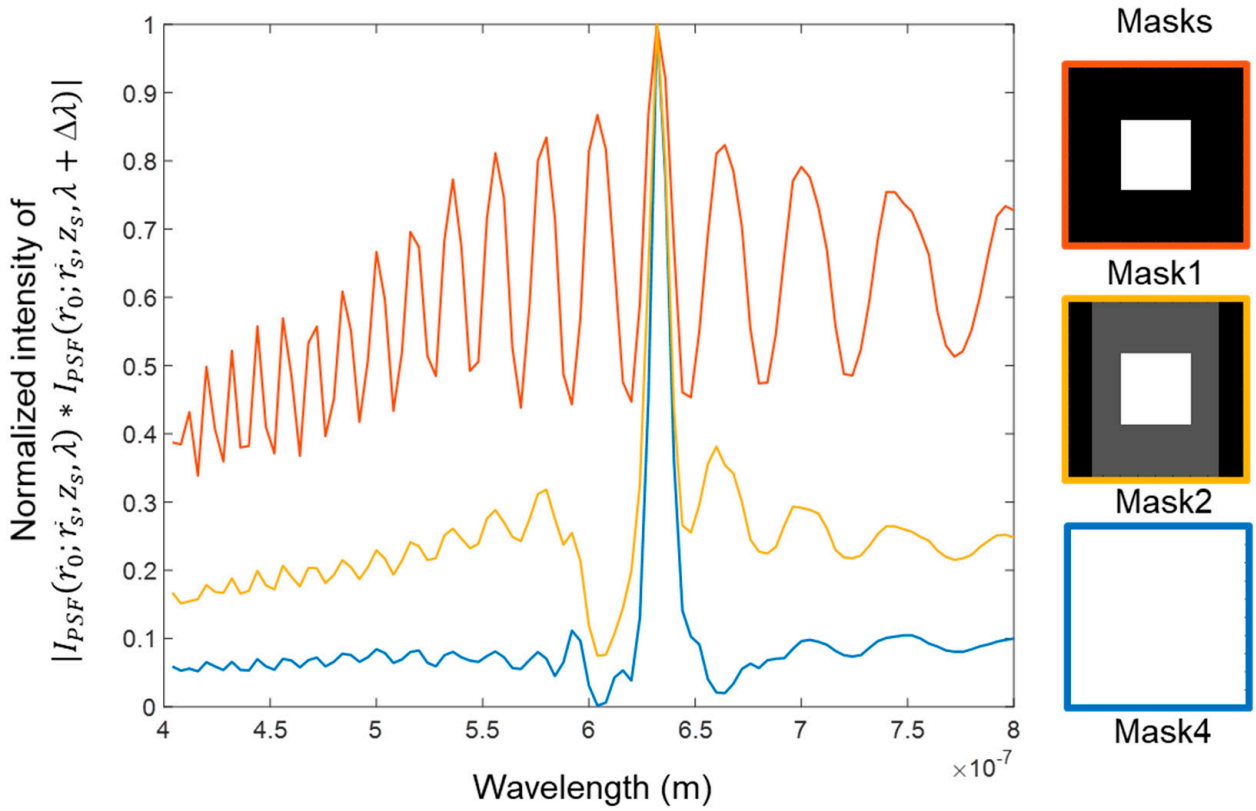

Figure 7. Simulation results of spectral correlation curves for different masks applied to the recorded I_{PSF} and I_{ROI}. The gray region in Mask2 has a ratio of 0.33 to the white region. The color of the curves are matched with the border color of the masks.

This tutorial also unifies the previous studies on this topic using a hybrid imaging system with a lens and an axicon and an Airy beam generator [27,28]. In this study, only two types of elements, namely a diffractive lens and a diffractive axicon, have been used. However, it is possible to use a wide range of diffractive elements and beams, such as self-rotating beams [25,38,39], Airy beams [40,41], and higher-order Bessel beams [42–44]. In this study, only three beams have been used; however, lesser or a greater number of beams can be used to achieve axial and spectral tunability post-recording.

6. Conclusions

Spatial ensemble mapping (SEM) has been introduced to the CAI technique. In SEM, different beams are mapped to different lateral locations in the image sensor. By this simple yet fundamental change, the imaging properties can be made flexible. The goal of SEM is to have different strengths of one or more imaging characteristics available as components of a parameter, and one or more components can be combined depending upon the requirements to obtain 'on-demand imaging' characteristics. In this study, three diffractive elements, namely two diffractive lenses and one diffractive axicon, were combined using the TAP-GSA to obtain a single phase-only diffractive element with minimal scattering. The diffraction patterns from the above three elements were positioned at different locations. A diffractive axicon has a long axial correlation length, whereas a diffractive lens has a short axial correlation length. Therefore, by combining diffraction patterns with different strengths, a desired correlation length can be engineered. In this study, only the LRRA and WD have been used, but any reconstruction algorithm such as NLR or INDIA can be used. This technique can be expanded and investigated for a wide range of optical beams, such as self-rotating beams [25], Airy beams [45], etc., tuning different parameters such as spectral resolution [46], lateral resolution [47,48], and 3D image steering [49,50].

One of the challenges that exists with CAI that precludes its application in commercial imaging systems is the lack of a robust computational reconstruction method that can reconstruct images with a high SNR. We believe that the developed SEM-CAI, with the development of advanced computational reconstruction methods, will benefit existing CAI techniques, I-COACH-based techniques, microscopy, and smartphone cameras [51–61]. While the developed technique has been demonstrated only with spatially incoherent light and for intensity imaging, it can be extended to coded aperture-based phase imaging applications [62–65].

Supplementary Materials: The following supporting information can be downloaded at: https://www.mdpi.com/article/10.3390/photonics11121174/s1, Supplementary_code1.txt and Supplementary_code2.txt.

Author Contributions: Conceptualization, V.A.; methodology, S.G., A.P.I.X., N.J., V.T. and V.A.; validation, V.A., V.T., N.J., A.P.I.X. and S.G.; resources, V.A.; writing—original draft preparation, all the authors; supervision, V.A.; funding acquisition, V.A. All authors have read and agreed to the published version of the manuscript.

Funding: This research was funded by the European Union's Horizon 2020 research and innovation program, grant agreement No. 857627 (CIPHR).

Institutional Review Board Statement: Not applicable.

Informed Consent Statement: Not applicable.

Data Availability Statement: Data can be obtained from the corresponding author upon reasonable request.

Conflicts of Interest: The authors declare no conflicts of interest.

References

1. Mait, J.N.; Euliss, G.W.; Athale, R.A. Computational imaging. *Adv. Opt. Photonics* **2018**, *10*, 409–483. [CrossRef]
2. Rosen, J.; Vijayakumar, A.; Kumar, M.; Rai, M.R.; Kelner, R.; Kashter, Y.; Bulbul, A.; Mukherjee, S. Recent advances in self-interference incoherent digital holography. *Adv. Opt. Photonics* **2019**, *11*, 1–66. [CrossRef]
3. Ables, J.G. Fourier transform photography: A new method for X-ray astronomy. *Proc. Astron. Soc.* **1968**, *1*, 172. [CrossRef]
4. Dicke, R.H. Scatter-hole cameras for X-rays and gamma rays. *Astrophys. J.* **1968**, *153*, L101. [CrossRef]
5. Mertz, L.; Young, N.O. Fresnel transformation of images. In *Proceedings of the ICO Conference on Optical Instruments and Techniques*; Habell, K.J., Ed.; Chapman and Hall: London, UK, 1962; pp. 305–310.
6. Fenimore, E.E.; Cannon, T.M. Coded aperture imaging with uniformly redundant arrays. *Appl. Opt.* **1978**, *17*, 337–347. [CrossRef]
7. Olmos, P.; Cid, C.; Bru, A.; Oller, J.C.; de Pablos, J.L.; Perez, J.M. Design of a modified uniform redundant-array mask for portable gamma cameras. *Appl. Opt.* **1992**, *31*, 4742–4750. [CrossRef] [PubMed]
8. Singh, A.K.; Pedrini, G.; Takeda, M.; Osten, W. Scatter-plate microscope for lensless microscopy with diffraction limited resolution. *Sci. Rep.* **2017**, *7*, 10687. [CrossRef] [PubMed]
9. Horner, J.L.; Gianino, P.D. Phase-only matched filtering. *Appl. Opt.* **1984**, *23*, 812–816. [CrossRef]
10. Woods, J.W.; Ekstrom, M.P.; Palmieri, T.M.; Twogood, R.E. Best linear decoding of random mask images. *IEEE Trans. Nucl. Sci.* **1975**, *22*, 379–383. [CrossRef]
11. Richardson, W.H. Bayesian-Based Iterative Method of Image Restoration. *J. Opt. Soc. Am.* **1972**, *62*, 55–59. [CrossRef]
12. Lucy, L.B. An iterative technique for the rectification of observed distributions. *Astron. J.* **1974**, *79*, 745. [CrossRef]
13. Vijayakumar, A.; Rosen, J. Interferenceless coded aperture correlation holography—A new technique for recording incoherent digital holograms without two-wave interference. *Opt. Express* **2017**, *25*, 13883–13896. [CrossRef] [PubMed]
14. Wagadarikar, A.; John, R.; Willett, R.; Brady, D. Single disperser design for coded aperture snapshot spectral imaging. *Appl. Opt.* **2008**, *47*, B44–B51. [CrossRef]
15. Rai, M.R.; Vijayakumar, A.; Rosen, J. Non-linear adaptive three-dimensional imaging with interferenceless coded aperture correlation holography (I-COACH). *Opt. Express* **2018**, *26*, 18143–18154. [CrossRef]
16. Anand, V.; Han, M.; Maksimovic, J.; Ng, S.H.; Katkus, T.; Klein, A.; Bambery, K.; Tobin, M.J.; Vongsvivut, J.; Juodkazis, S. Single-shot mid-infrared incoherent holography using Lucy-Richardson-Rosen algorithm. *Opto-Electron. Sci.* **2022**, *1*, 210006.
17. Rosen, J.; Anand, V. Incoherent nonlinear deconvolution using an iterative algorithm for recovering limited-support images from blurred digital photographs. *Opt. Express* **2024**, *32*, 1034–1046. [CrossRef] [PubMed]
18. Anand, V.; Ng, S.H.; Maksimovic, J.; Linklater, D.; Katkus, T.; Ivanova, E.P.; Juodkazis, S. Single shot multispectral multidimensional imaging using chaotic waves. *Sci. Rep.* **2020**, *10*, 13902. [CrossRef] [PubMed]

19. Rai, M.R.; Vijayakumar, A.; Rosen, J. Extending the field of view by a scattering window in I-COACH system. *Opt. Lett.* **2018**, *43*, 1043–1046. [CrossRef]
20. Bulbul, A.; Vijayakumar, A.; Rosen, J. Superresolution far-field imaging by coded phase reflectors distributed only along the boundary of synthetic apertures. *Optica* **2018**, *5*, 1607–1616. [CrossRef]
21. Rai, M.R.; Vijayakumar, A.; Ogura, Y.; Rosen, J. Resolution Enhancement in Nonlinear Interferenceless COACH with a Point Response of Subdiffraction Limit Patterns. *Opt. Express* **2019**, *27*, 391–403. [CrossRef]
22. Tamm, O.; Tiwari, V.; Gopinath, S.; Rajesway, A.S.J.F.; Singh, S.A.; Rosen, J.; Anand, V. Super-Resolution Correlating Optical Endoscopy. *IEEE Access* **2024**, *12*, 76955–76962. [CrossRef]
23. Rai, M.R.; Rosen, J. Depth-of-field engineering in coded aperture imaging. *Opt. Express* **2021**, *29*, 1634–1648. [CrossRef]
24. Anand, V. Tuning Axial Resolution Independent of Lateral Resolution in a Computational Imaging System Using Bessel Speckles. *Micromachines* **2022**, *13*, 1347. [CrossRef]
25. Kumar, R.; Vijayakumar, A.; Rosen, J. 3D single shot lensless incoherent optical imaging using coded phase aperture system with point response of scattered airy beams. *Sci. Rep.* **2023**, *13*, 2996. [CrossRef] [PubMed]
26. Bleahu, A.; Gopinath, S.; Kahro, T.; Angamuthu, P.P.; Rajeswary, A.S.J.F.; Prabhakar, S.; Kumar, R.; Salla, G.R.; Singh, R.P.; Kukli, K.; et al. 3D Incoherent Imaging Using an Ensemble of Sparse Self-Rotating Beams. *Opt. Express* **2023**, *31*, 26120–26134. [CrossRef]
27. Gopinath, S.; Rajeswary, A.S.J.F.; Anand, V. Sculpting axial characteristics of incoherent imagers by hybridization methods. *Opt. Lasers Eng.* **2024**, *172*, 107837. [CrossRef]
28. Gopinath, S.; Anand, V. Post-ensemble generation with Airy beams for spatial and spectral switching in incoherent imaging. *Opt. Lett.* **2024**, *49*, 3247–3250. [CrossRef]
29. Gopinath, S.; Bleahu, A.; Kahro, T.; Rajeswary, A.S.J.F.; Kumar, R.; Kukli, K.; Tamm, A.; Rosen, J.; Anand, V. Enhanced design of multiplexed coded masks for Fresnel incoherent correlation holography. *Sci. Rep.* **2023**, *13*, 7390. [CrossRef] [PubMed]
30. Rosen, J.; Brooker, G. Digital spatially incoherent Fresnel holography. *Opt. Lett.* **2007**, *32*, 912–914. [CrossRef] [PubMed]
31. Katz, B.; Rosen, J.; Kelner, R.; Brooker, G. Enhanced resolution and throughput of Fresnel incoherent correlation holography (FINCH) using dual diffractive lenses on a spatial light modulator (SLM). *Opt. Express* **2012**, *20*, 9109–9121. [CrossRef]
32. Rosen, J.; Alford, S.; Allan, B.; Anand, V.; Arnon, S.; Arockiaraj, F.G.; Art, J.; Bai, B.; Balasubramaniam, G.M.; Birnbaum, T.; et al. Roadmap on computational methods in optical imaging and holography. *Appl. Phys. B* **2024**, *130*, 166. [CrossRef] [PubMed]
33. Golub, I. Fresnel axicon. *Opt. Lett.* **2006**, *31*, 1890–1892. [CrossRef] [PubMed]
34. McLeod, J. The Axicon: A new type of optical element. *J. Opt. Soc. Am.* **1954**, *44*, 592–597. [CrossRef]
35. Khonina, S.N.; Kazanskiy, N.L.; Khorin, P.A.; Butt, M.A. Modern Types of Axicons: New Functions and Applications. *Sensors* **2021**, *21*, 6690. [CrossRef]
36. Khonina, S.N.; Porfirev, A.P. 3D transformations of light fields in the focal region implemented by diffractive axicons. *Appl. Phys. B* **2018**, *124*, 191. [CrossRef]
37. Khonina, S.N.; Volotovsky, S.G. Application axicons in a large-aperture focusing system. *Opt. Mem. Neural Netw.* **2014**, *23*, 201–217. [CrossRef]
38. Niu, K.; Zhao, S.; Liu, Y.; Tao, S.; Wang, F. Self-rotating beam in the free space propagation. *Opt. Express* **2022**, *30*, 5465–5472. [CrossRef]
39. Niu, K.; Zhai, Y.; Wang, F. Self-healing property of the self-rotating beam. *Opt. Express* **2022**, *30*, 30293–30302. [CrossRef]
40. Siviloglou, G.A.; Broky, J.; Dogariu, A.; Christodoulides, D.N. Observation of accelerating Airy beams. *Phys. Rev. Lett.* **2007**, *99*, 213901. [CrossRef] [PubMed]
41. Vettenburg, T.; Dalgarno, H.I.C.; Nylk, J.; Coll-Lladó, C.; Ferrier, D.E.K.; Cizmar, T.; Gunn-Moore, F.J.; Dholakia, K. Light-sheet microscopy using an Airy beam. *Nat. Methods* **2014**, *11*, 541–544. [CrossRef]
42. Tudor, R.; Bulzan, G.A.; Kusko, M.; Kusko, C.; Avramescu, V.; Vasilache, D.; Gavrila, R. Multilevel Spiral Axicon for High-Order Bessel–Gauss Beams Generation. *Nanomaterials* **2023**, *13*, 579. [CrossRef]
43. He, C.; Shen, Y.; Forbes, A. Towards Higher-Dimensional Structured Light. *Light Sci. Appl.* **2022**, *11*, 205. [CrossRef]
44. Arlt, J.; Dholakia, K. Generation of High-Order Bessel Beams by Use of an Axicon. *Opt. Commun.* **2000**, *177*, 297–301. [CrossRef]
45. Yang, L.; Yang, J.; Huang, T.; Rosen, J.; Wang, Y.; Wang, H.; Lu, X.; Zhang, W.; Di, J.; Zhong, L. Accelerating quad Airy beams-based point response for interferenceless coded aperture correlation holography. *Opt. Lett.* **2024**, *49*, 4429–4432. [CrossRef]
46. Sahoo, S.K.; Tang, D.; Dang, C. Single-shot multispectral imaging with a monochromatic camera. *Optica* **2017**, *4*, 1209. [CrossRef]
47. Jiang, Y.; Liu, Y.; Zhan, W.; Zhu, D. Improved Thermal Infrared Image Super-Resolution Reconstruction Method Base on Multimodal Sensor Fusion. *Entropy* **2023**, *25*, 914. [CrossRef]
48. Zou, Y.; Zhang, L.; Liu, C.; Wang, B.; Hu, Y.; Chen, Q. Super-resolution reconstruction of infrared images based on a convolutional neural network with skip connections. *Opt. Lasers Eng.* **2021**, *146*, 106717. [CrossRef]
49. Balasubramani, V.; Lai, X.J.; Lin, Y.C.; Cheng, C.J. Integrated dual-tomography for refractive index analysis of free-floating single living cell with isotropic superresolution. *Sci. Rep.* **2018**, *8*, 5943.
50. Balasubramani, V.; Kuś, A.; Tu, H.Y.; Cheng, C.J.; Baczewska, M.; Krauze, W.; Kujawińska, M. Holographic tomography: Techniques and biomedical applications [Invited]. *Appl. Opt.* **2021**, *60*, B65–B80. [CrossRef]
51. García-Sánchez, I.; Fresnedo, Ó.; González-Coma, J.P.; Castedo, L. Coded Aperture Hyperspectral Image Reconstruction. *Sensors* **2021**, *21*, 6551. [CrossRef]

52. Zhao, T.; Wu, Q.; Zhao, F.; Xu, Z.; Xiao, S. A Full-Polarization Radar Image Reconstruction Method with Orthogonal Coding Apertures. *Remote Sens.* **2021**, *13*, 4626. [CrossRef]
53. Chen, S.; Luo, C.; Wang, H.; Deng, B.; Cheng, Y.; Zhuang, Z. Three-Dimensional Terahertz Coded-Aperture Imaging Based on Matched Filtering and Convolutional Neural Network. *Sensors* **2018**, *18*, 1342. [CrossRef]
54. Peng, L.; Luo, C.; Deng, B.; Wang, H.; Qin, Y.; Chen, S. Phaseless Terahertz Coded-Aperture Imaging Based on Incoherent Detection. *Sensors* **2019**, *19*, 226. [CrossRef]
55. Peng, L.; Luo, C.; Deng, B.; Wang, H.; Chen, S.; Dong, J. Phaseless Terahertz Coded-Aperture Imaging for Sparse Target Based on Phase Retrieval Algorithm. *Sensors* **2019**, *19*, 4617. [CrossRef]
56. Chen, S.; Hua, X.; Wang, H.; Luo, C.; Cheng, Y.; Deng, B. Three-Dimensional Terahertz Coded-Aperture Imaging Based on Geometric Measures. *Sensors* **2018**, *18*, 1582. [CrossRef]
57. Wang, J.; Zhao, Y. Lensless Multispectral Camera Based on a Coded Aperture Array. *Sensors* **2021**, *21*, 7757. [CrossRef]
58. Xiong, R.; Zhang, X.; Ma, X.; Qi, L.; Li, L.; Jiang, X. Enhancement of Imaging Quality of Interferenceless Coded Aperture Correlation Holography Based on Physics-Informed Deep Learning. *Photonics* **2022**, *9*, 967. [CrossRef]
59. Gan, F.; Yuan, Z.; Luo, C.; Wang, H. Phaseless Terahertz Coded-Aperture Imaging Based on Deep Generative Neural Network. *Remote Sens.* **2021**, *13*, 671. [CrossRef]
60. Rosen, J. Advanced Imaging Methods Using Coded Aperture Digital Holography. *Eng. Proc.* **2023**, *34*, 2. [CrossRef]
61. Meißner, T.; Rozhkov, V.; Hesser, J.; Nahm, W.; Loew, N. Quantitative comparison of planar coded aperture imaging reconstruction methods. *J. Instrum.* **2023**, *18*, P01006. [CrossRef]
62. Hai, N.; Rosen, J. Interferenceless and motionless method for recording digital holograms of coherently illuminated 3D objects by coded aperture correlation holography system. *Opt. Express* **2019**, *27*, 24324–24339. [CrossRef]
63. Hai, N.; Rosen, J. Doubling the acquisition rate by spatial multiplexing of holograms in coherent sparse coded aperture correlation holography. *Opt. Lett.* **2020**, *45*, 3439–3442. [CrossRef]
64. Rosen, J.; Bulbul, A.; Hai, N.; Rai, M.R. Coded aperture correlation holography (COACH)—A research journey from 3D incoherent optical imaging to quantitative phase imaging. In *Holography—Recent Advances and Applications*; IntechOpen: London, UK, 2023.
65. Hai, N.; Rosen, J. Single viewpoint tomography using point spread functions of tilted pseudo-nondiffracting beams in interferenceless coded aperture correlation holography with nonlinear reconstruction. *Opt. Laser Technol.* **2023**, *167*, 109788. [CrossRef]